

Microfluidic channels with ultralow-loss waveguide crossings for various chip-integrated photonic sensors

Zheng Wang,^{1,2,6} Hai Yan,² Swapnajit Chakravarty,^{3,7} Harish Subbaraman,³ Xiaochuan Xu,³
D.L. Fan,^{1,4} Alan X. Wang,⁵ and Ray T. Chen^{1,2,3,*}

¹Materials Science and Engineering Program, Texas Materials Institute, The University of Texas at Austin, Austin, Texas 78712, USA

²Department of Electrical and Computer Engineering, The University of Texas at Austin, 10100 Burnet Rd., MER 160, Austin, Texas 78758, USA

³Omega Optics, Inc., 8500 Shoal Creek Blvd., Bldg. 4, Suite 200, Austin, Texas 78757, USA

⁴Department of Mechanical Engineering, University of Texas at Austin, Austin, Texas 78712, USA

⁵School of Electrical Engineering and Computer Science, Oregon State University, Corvallis, Oregon 97331, USA

⁶e-mail: wangzheng@utexas.edu

⁷e-mail: swapnajit.chakravarty@omegaoptics.com

*Corresponding author: raychen@uts.cc.utexas.edu

Received January 19, 2015; revised March 13, 2015; accepted March 14, 2015;
posted March 16, 2015 (Doc. ID 232699); published March 30, 2015

Traditional silicon waveguides are defined by waveguide trenches on either side of the high-index silicon core that leads to fluid leakage orifices for over-layed microfluidic channels. Closing the orifices needs additional fabrication steps which may include oxide deposition and planarization. We experimentally demonstrated a new type of microfluidic channel design with ultralow-loss waveguide crossings (0.00248 dB per crossings). The waveguide crossings and all other on-chip passive-waveguide components are fabricated in one step with no additional planarization steps which eliminates any orifices and leads to leak-free fluid flow. Such designs are applicable in all optical-waveguide-based sensing applications where the analyte must be flowed over the sensor. The new channel design was demonstrated in a L55 photonic crystal sensor operating between 1540 and 1580 nm. © 2015 Optical Society of America

OCIS codes: (280.0280) Remote sensing and sensors; (050.5298) Photonic crystals.
<http://dx.doi.org/10.1364/OL.40.001563>

Microfluidic channel systems have shown unique advantages in performing analytical functions such as controlled transportation, immobilization, and manipulation of biological molecules and have become an essential part of modern nanotechnology research [1]. On the other hand, chip-integrated photonic sensors, utilizing microring resonators [2], 2D photonic crystal [3], wire waveguides [4], etc., have enabled label-free and high-sensitivity sensing with ultra-compact size and low cost. By integrating microfluidics with photonic sensors, one may gain more benefits like reduced sample consumption, shorter analysis time, higher sensitivity, and portability, etc. More importantly, microfluidic channel system is a necessary technique for achieving integrated biosensors [5]. Our previous work has already demonstrated high-sensitivity photonic-crystal chemical sensors [6], enhanced-sensitivity photonic-crystal biosensors [7], and plasmonic-active surface-enhanced Raman spectroscopy systems [8]. While sensing characteristics can in general be demonstrated by dispensing analytes of interest via pipettes, when binding kinetics need to be measured for instance in the case of biosensors for drug discovery applications, a continuous flow of analyte must be reliably achieved.

A conventional optical waveguide is characterized by cross-section such as J-J' shown in Fig. 1(a). Optical waveguides are in general layed out such that the fluids flow orthogonal to the direction of optical wave propagation. Thus, as noted in the right image in Fig. 1(b), an air gap would exist between the PDMS layer (PDMS

being the material of choice for microfluidic channels) and the bottom silicon dioxide cladding in a silicon-on-insulator (SOI) substrate. One typical solution to close the avenue for fluid leakage in silicon-chip-integrated waveguide sensor is introducing additional fabrication steps including but not limited to oxide deposition followed by planarization and selective oxide removal prior to microfluidic channel bonding [9]. In the case of photonic-crystal sensors, such post-processing would necessitate removal of the oxide from the etched photonic-crystal patterns, which would result in additional etching of the bottom oxide cladding unless the process is very strictly controlled. A poor tolerance on the oxide removal processing would lead to uncertain resonance wavelengths in photonic-crystal biosensors.

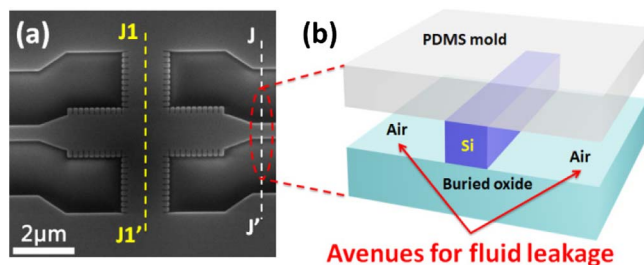


Fig. 1. (a) SEM image of a typical waveguide crossing. Conventional waveguides are characterized by cross-sections J-J' and waveguide crossings are labeled by J1-J1'. (b) Cross-sectional view of the PDMS microfluidic channel when integrated with optical waveguides in silicon in a SOI substrate.

Recently, photonic-crystal devices have been fabricated using photolithography [10]. However, additional fabrication steps associated with oxide deposition, planarization, and removal need additional photo masks, which translate to higher manufacturing cost.

In this Letter, we demonstrate an approach using ultra-low-loss silicon waveguide crossings to build a closed microfluidic channel with leak-free integrated fluidics operation. The microfluidic channel is designed so that channel walls go over the section J1-J1' in Fig. 1(a) which effectively closes the gaps that would otherwise exist in the channel along J-J', in the absence of waveguide crossings. This novel approach is fabrication friendly, since the primary ridge waveguides, photonic crystals, and crossing waveguides are fabricated in the same step with a single photomask, and also offers a smooth interface excluding additional planarization process for microfluidic channel bonding.

A cascaded MMIs structure, whose top-view schematic is shown in Fig. 2(a), is utilized to build ultra-low-loss

waveguide crossings on a SOI substrate (3- μm -thick buried oxide layer and 250-nm-thick top silicon layer) since it enables guiding of low-loss Bloch waves by periodic self-focusing sections offered by MMIs [11]. Commercially available software FIMMWAVE (developed by Photon Design Ltd.) is used for simulation, and a side view schematic of the simulated structure is shown Fig. 2(b). Here the W_{si} is chosen to be 0.6 μm to build a single-mode waveguide, and W_{mmi} is chosen as 1.2 μm to support only three quasi-TE modes (zeroth, first, and second). As the symmetry of this structure, the odd first-order mode has not been excited. Hence the self-focusing condition can be perfectly fulfilled by tuning L_{in} and L_{s} to eliminate the phase error between zeroth and second mode. Linear tapers ($L_t = 1 \mu\text{m}$) are added to avoid sharp transition and at the same time to reduce the portion of the power in second-order mode in the MMI region that could improve the power transition [12]. Effective medium theory is utilized to calculate the cladding index (n_c) around the crossing region which provides a minimal modal phase noise, thus lowering the propagation loss at the crossing region. Theoretically, one can drive the phase error of the m th mode $\Delta\varphi_m$ at the N-folding imaging length as

$$\Delta\varphi_m \approx \frac{P \lambda_0^2 (m+1)^4 \pi}{4 \cdot 2N n_f^2 W_{e0}^2} \left[\frac{1}{8} - \frac{\lambda_0 n_f^2}{6\pi W_{e0} (n_f^2 - n_c^2)^2} \right], \quad (1)$$

where P is the number of self-imaging periods, λ_0 is the optical wavelength, W_{e0} is the effective width of the MMI for the zeroth mode, n_f is the effective refractive index of the fundamental mode of infinite slab waveguides with the same thickness as the MMI, and n_c is the lateral cladding index [11]. Specifically speaking, the increasing of n_c will reduce the TM component of quasi-TE mode both in single-mode ridge waveguide and MMI region. Thus the power transition between the two waveguides will be improved at the input and output. Figure 2(c) shows a scan of the cladding index (n_c), which indicates that $n_c \sim 2.5$ is sufficient to provide the lowest loss result. The propagation field profile of 20 waveguide crossings with the optimized parameters: $n_c \sim 2.5$, $L_{\text{in}} = 2.16 \mu\text{m}$, $L_{\text{s}} = 1.58 \mu\text{m}$ is shown in Fig. 2(d), and the propagation loss is 0.0241 dB per crossing. The measured experimental loss is 0.0248 dB per crossing. SEM images of fabricated waveguide crossings are shown in Figs. 2(e)–2(g). Those tooth-like subwavelength nanostructures are used to make an artificial material with desired lateral cladding index $n_c \sim 2.5$ [13].

In order to demonstrate the effectiveness of the waveguide crossings in preventing the leaking problem as well as its compatibility with photonic sensors, we integrate waveguide crossings with our matured L55 photonic crystal microcavity sensor [14]. The 3D schematic of the integrated device, which the PMDS-based microfluidic channel has already been bonded onto the sensor chip, is shown in Fig. 3(a) and an exploded view 3D schematic illustrating components of the integrated device is shown in Fig. 3(b). The photonic crystal microcavity sensor sits in the center integrated with the primary ridge waveguide. Waveguide crossings are located on both sides of the photonic crystal sensor where the PDMS wall

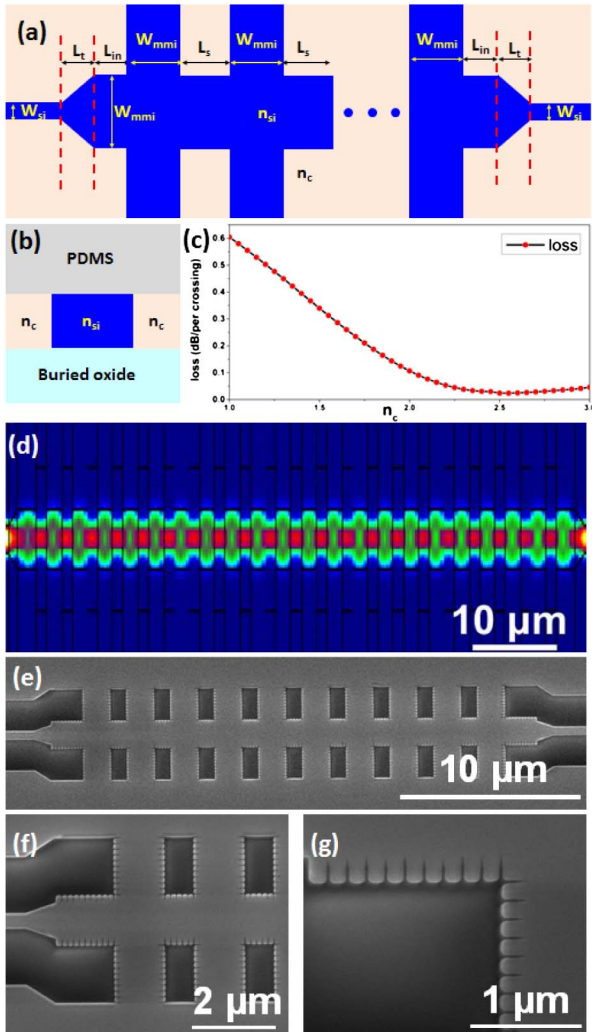


Fig. 2. (a) Top-view schematic of cascaded MMI-based waveguide crossings. (b) Side view schematic of simulated structure. (c) Simulated propagation loss versus lateral cladding index for the structure in (a). (d) FIMMWAVE simulation result of 20 waveguide crossings with optimized parameters. (e)–(g) SEM images of fabricated waveguide crossings.

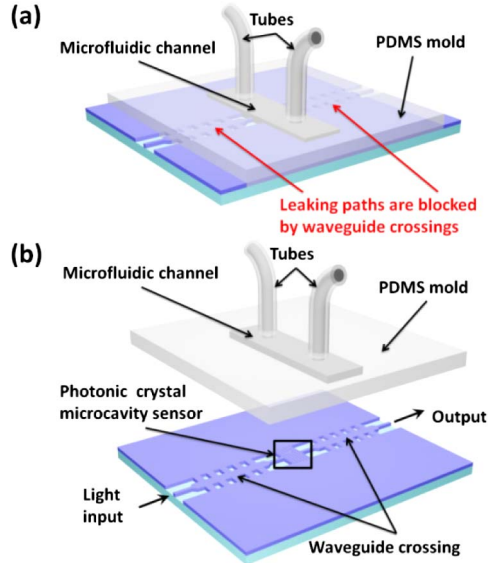


Fig. 3. (a) 3D schematic of the integrated device. (b) Exploded view 3D schematic of the integrated device.

of the microfluidic channel is placed. Subwavelength gratings [15] are used to couple light in and out between silicon waveguide and optical fibers.

All structures, including primary ridge waveguides, photonic crystal waveguides and microcavity, waveguide crossings, and subwavelength grating couplers, are patterned in one E-beam lithography step. The pattern was then transferred to silicon layer through reactive-ion-etch (RIE). The microfluidic channel was fabricated using polydimethylsiloxane (PDMS) following standard soft lithography technique [16]. Briefly, a 50- μm -thick SU-8 photoresist was spin-coated on a silicon wafer. The microfluidic channel pattern was transferred to the photoresist layer using photolithography through a Mylar mask. After development, a SU-8 layer is used to mold PDMS. PDMS was poured on to a polished Si wafer and polymerized in an oven at 70°C for 2 h. Later, two holes were punctured at each end of the microfluidic channel as inlet and outlet ports for tubes connection. The microfluidic channel fabricated is 1 mm wide and 15 mm long. The PDMS layer with fabricated microfluidic channel aligned with the sensor chip is shown in Fig. 4(a). Here we use pressure-bonding technique inspired by Quan *et al.* [17]. For biosensing, PDMS is accepted universally as a biocompatible microfluidic channel material. However, PDMS cannot serve as a channel material for organic solvents. Furthermore, new materials are being designed as an alternative to PDMS to achieve better wetting characteristics of channel walls. The use of pressure bonding allows any suitable choice of microfluidic channel material other than PDMS, without the need for new process development. The PDMS layer with microfluidic channel was aligned to the silicon chip and then clamped together by two pieces of laser-cut acrylic glass. The sensor chip integrated with microfluidic channel and clamps were placed on an optical stage for fiber to grating coupler alignment and transmission spectrum measurement. The setup is shown in Fig. 4(b). Solution was introduced into the channel by

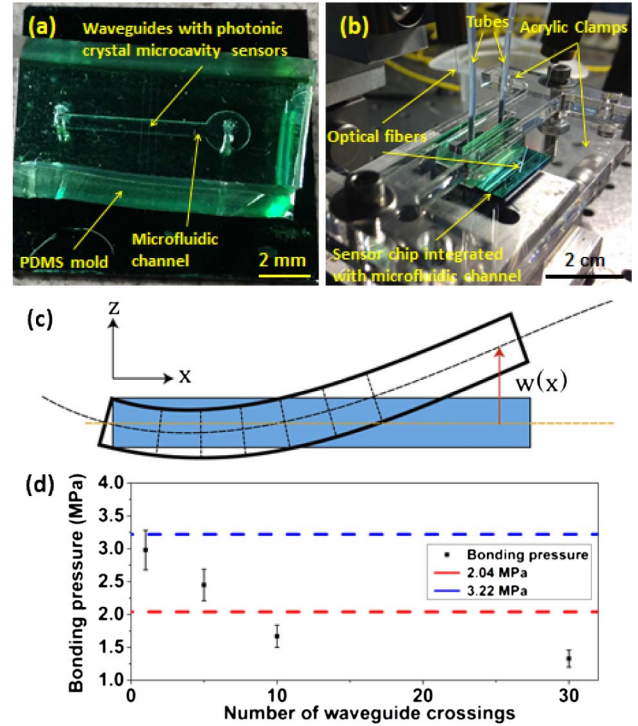


Fig. 4. (a) Picture of a device with PDMS microfluidic channel. (b) Picture of the measurement setup. (c) Coordinate system for break stress calculation (d) Bonding pressure between PDMS layer and silicon waveguide crossings. Dashed lines indicate the upper and lower limits of break stress in acrylic clamps.

a syringe pump (Harvard Apparatus). Light from a LED source (DenseLight Semiconductors) was coupled into the sensor waveguide through a grating coupler to stimulate quasi-TE mode. On the output port, light was coupled out into an optical spectrum analyzer to obtain the transmission spectrum.

Different numbers of waveguide crossings 1, 5, 10, and 30 on both sides are fabricated to test the necessary bonding pressure for a leak-free system. Using Euler–Bernoulli beam theory, the relationship between the deflection of the beam and bonding pressure between PDMS and silicon waveguide crossings can be obtained as

$$w(x) = \frac{PS}{6EI} (3Lx^2 - x^3), \quad (2)$$

where $w(x)$ is the deflection, P is the bonding pressure, S is the area between acrylic beam and PDMS layer, E is the elastic modulus, and I is the second moment of area. The coordinate system is shown in Fig. 4(c), and bonding pressure calculated from deflection is shown in Fig. 4(d).

The maximum stress in a beam at a given bonding pressure can be calculated with

$$\sigma_{\max} = \frac{I}{h} \iiint P x dx ds. \quad (3)$$

The break strength of acrylic (ISO 527-2) is approximately 48.95–77.22 MPa. Thus the limits of bonding pressure are about 2.04–3.22 MPa, which is calculated with

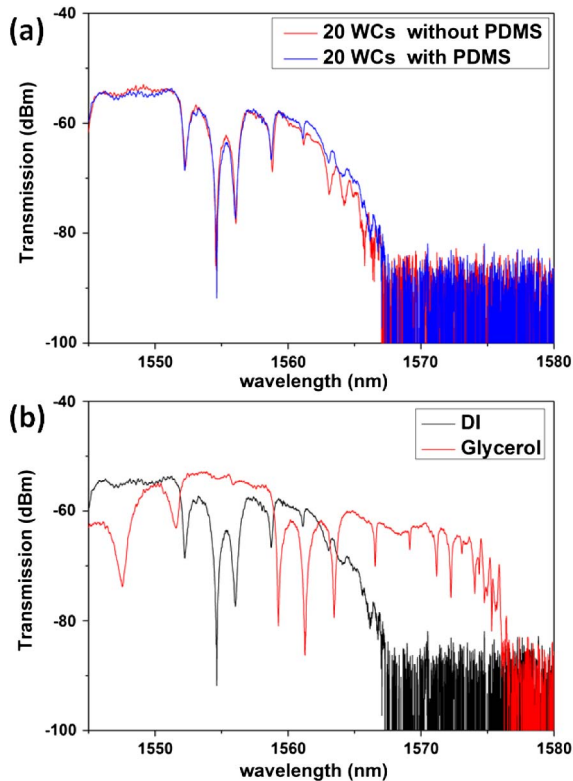


Fig. 5. (a) Spectra of L55 photonic crystal microcavity sensor with 10 waveguide crossings on both sides with and without PDMS microfluidic channel. (b) Spectra of L55 photonic crystal microcavity sensor tested in DI water and glycerol.

(3) and plotted as the two dashed lines in Fig. 4(d). Mechanical failures in the acrylic clamps are observed for devices with 1 and 5 waveguide crossings. To avoid the mechanical failure of acrylic clamps, 10 waveguide crossings with calculated 1.84-MPa bonding pressure is selected for the experiments.

Considering that PDMS absorbance is about 3 dB/cm in the wavelength range 1540–1580 nm [18], the devices first were tested in DI-water without and with PDMS layer to show the effect caused by PDMS absorption. Transmission spectra were shown in Fig. 5(a) and strong resonance peaks are observed. The propagation loss caused by the PDMS layer could be neglected as the planar favored energy distribution of quasi-TE mode. The same device was next tested in glycerol to validate operation as a chemical sensor. Experiment results are shown in Fig. 5(b). The shift of the transmission spectrum is 7.1 nm corresponding to the refractive index change [19].

In conclusion, we integrated waveguide crossings into the chip-based waveguide sensor that enables leak-free operation of microfluidic channels. This process is

compatible with existing SOI micro-fabrication technique and requires no additional fabrication step. Also this scheme is suitable for various sensing application that uses optical waveguides and need microfluidic channel to deliver the media to be tested.

The authors acknowledge the National Institutes of Health for sponsoring this research under SBIR grant no. 5R42 ES024023-03 and Dr. Zongxing Wang's help.

References

1. J. W. Hong and S. R. Quake, *Nat. Biotechnol.* **21**, 1179 (2003).
2. A. L. Washburn, L. C. Gunn, and R. C. Bailey, *Anal. Chem.* **81**, 9499 (2009).
3. S. Pal, E. Guillermain, R. Sriram, B. L. Miller, and P. M. Fauchet, *Biosens. Bioelectron.* **26**, 4024 (2011).
4. A. Densmore, M. Vachon, D. X. Xu, S. Janz, R. Ma, Y. H. Li, G. Lopinski, A. Delage, J. Lapointe, C. C. Luebbert, Q. Y. Liu, P. Cheben, and J. H. Schmid, *Opt. Lett.* **34**, 3598 (2009).
5. D. Erickson and D. Q. Li, *Ana. Chim. Acta.* **507**, 11 (2004).
6. W. C. Lai, S. Chakravarty, Y. Zou, and R. T. Chen, *Opt. Lett.* **38**, 3799 (2013).
7. W. C. Lai, S. Chakravarty, Y. Zou, Y. B. Guo, and R. T. Chen, *Appl. Phys. Lett.* **102**, 041111 (2013).
8. X. B. Xu, D. H. Hasan, L. Wang, S. Chakravarty, R. T. Chen, D. L. Fan, and A. X. Wang, *Appl. Phys. Lett.* **100**, 191114 (2012).
9. J. M. Ruano, V. Benoit, J. S. Aitchison, and J. M. Cooper, *Anal. Chem.* **72**, 1093 (2000).
10. C.-J. Yang, N. Tang, H. Yan, S. Chakravarty, D. Li, and R. Chen, "193 nm lithography fabricated high sensitivity photonic crystal microcavity biosensors for plasma protein detection in patients with pancreatic cancer," in *CLEO* (to be published).
11. Y. Zhang, A. Hosseini, X. C. Xu, D. Kwong, and R. T. Chen, *Opt. Lett.* **38**, 3608 (2013).
12. C. H. Chen and C. H. Chiu, *IEEE J. Quantum Electron.* **46**, 1656 (2010).
13. A. Ortega-Monux, L. Zavargo-Peche, A. Maese-Novo, I. Molina-Fernandez, R. Halir, J. G. Wangumert-Perez, P. Cheben, and J. H. Schmid, *IEEE Photon. Tech. Lett.* **23**, 1406 (2011).
14. Y. Zou, S. Chakravarty, D. N. Kwong, W. C. Lai, X. C. Xu, X. H. Lin, A. Hosseini, and R. T. Chen, *IEEE J. Sel. Top. Quantum Electron.* **20**, 171 (2014).
15. X. C. Xu, H. Subbaraman, J. Covey, D. Kwong, A. Hosseini, and R. T. Chen, *Appl. Phys. Lett.* **101**, 031109 (2012).
16. M. A. Unger, H. P. Chou, T. Thorsen, A. Scherer, and S. R. Quake, *Science* **288**, 113 (2000).
17. D. Q. Yang, S. Kita, F. Liang, C. Wang, H. P. Tian, Y. F. Ji, M. Loncar, and Q. M. Quan, *Appl. Phys. Lett.* **105**, 063118 (2014).
18. D. K. Cai, A. Neyer, R. Kuckuk, and H. M. Heise, *Opt. Mater.* **30**, 1157 (2008).
19. S. Chakravarty, A. Hosseini, X. C. Xu, L. Zhu, Y. Zou, and R. T. Chen, *Appl. Phys. Lett.* **104**, 191109 (2014).